Study on CO_2 and CH_4 Competitive Adsorption in Shale Organic and Clay Porous Media from Molecular- to Pore-Scale Simulation

Han Wang[1] ⓘ, Jinsong Huang[2], Shiyuan Zhan[3], Mingshan Zhang[4]* ⓘ, and Jianchao Cai[1] ⓘ

[1]National Key Laboratory of Petroleum Resources and Engineering, China University of Petroleum, Beijing
[2]CNOOC EnerTech-Drilling & Production Co.
[3]College of Energy, Chengdu University of Technology
[4]Key Laboratory of Ministry of Education on Safe Mining of Deep Metal Mines, School of Resources and Civil Engineering, Northeastern University

Summary

The elucidation of the competitive adsorption behaviors between CO_2 and CH_4 holds great importance in the context of improving natural gas recovery in shale reservoirs. Shale rock, as a complex porous medium, exhibits a highly interconnected multiscale pore network with pore size spanning from several to tens of nanometers. Nevertheless, accurately capturing the adsorption effects and studying the CO_2/CH_4 competitive adsorption within a large-scale, realistic, 3D nanoporous matrix remains a significant challenge. In this paper, we proposed a novel lattice Boltzmann method (LBM) coupled molecular simulation to investigate CO_2/CH_4 competitive adsorption in 3D shale nanoporous media. The initial step involves conducting Grand Canonical Monte Carlo (GCMC) simulations to simulate the competitive adsorption behaviors of CO_2 and CH_4 in kerogen and illite slit pores, with the aim of obtaining the atomic density distribution. Subsequently, a Shan-Chen-based lattice Boltzmann (LB) simulation is used under identical conditions. By coupling the molecular simulation results, the fluid-solid interaction parameters are determined. Finally, LB simulations are performed in designed 3D porous media, utilizing the fluid-solid interaction parameters. The effects of mineral type, CO_2 concentration, and pore structure on competitive adsorption behaviors are discussed carefully. Our research offers significant contributions to the improvement of gas recovery and carbon geological sequestration through the examination of CO_2/CH_4 competitive adsorption in nanoporous media. Additionally, it serves as a link between molecular and pore-scale phenomena by leveraging the benefits of both molecular simulations and pore-scale simulations.

Introduction

With the breakthrough in horizontal drilling and hydraulic fracturing technologies, unconventional natural gas in shale reservoirs is playing an ever-increasing role in addressing the challenge of the global energy crisis, owing to the large reserve potentials and high energy efficiency (Wang et al. 2014; Cooper et al. 2016; Middleton et al. 2017). In contrast to conventional gas reservoirs, shale reservoirs contain a significant number of nanopores with pore sizes ranging from several to hundreds of angstroms, which are widely distributed (Chalmers et al. 2012; Zhang et al. 2019). This distribution results in strong surface adsorption effects (Ross and Bustin 2009; Pang et al. 2019; Zhou et al. 2022a; Bekeshov et al. 2023). It is reported that adsorbed CH_4 in shale could account for up to 85% of total gas in place, greatly affecting the gas storage capacity evaluation and production efficiency (Curtis 2002). Generally, the primary recovery factor for most shale gas reservoirs is less than 25%, and a large proportion of shale gas remains trapped underground (Kuuskraa et al. 2013; Cooper et al. 2016). CO_2 injection has been recognized as an effective and promising technique capable of enhancing gas recovery while achieving carbon geological sequestration (CGS) simultaneously (Jung et al. 2010; Sun et al. 2017; Lyu et al. 2021; Safaei-Farouji et al. 2023; Wang et al. 2023b). This is mainly due to the preferential adsorption capacity of CO_2 over CH_4 on rock surfaces (Zhou et al. 2018; Klewiah et al. 2020). On the other hand, shale formation is a heterogeneous mixture of organic (kerogen) and inorganic (clay, quartz, carbonate, etc.) matter, creating a complex pore network in shale reservoirs (Chalmers et al. 2012; Li and Elsworth 2019). Therefore, it is essential to study the competitive adsorption behaviors of CO_2 and CH_4 in nanoporous shale matrices to accurately predict CH_4 recovery efficiency and optimize on-site CO_2 injection strategies.

To date, significant efforts have been dedicated to comprehending the competitive adsorption characteristics of CO_2 and CH_4 in shale reservoirs through laboratory adsorption testing, in which the adsorption capacity, adsorption selectivity, and isosteric heats are carefully examined and discussed (Liu et al. 2019; Zhang et al. 2022; Xie et al. 2022; Qin et al. 2022; Liao et al. 2023; Wu et al. 2023b). The results revealed that CO_2 presents greater adsorption amount and affinity than CH_4, justifying the feasibility of CO_2 injection in enhanced gas recovery (EGR) associated with the CGS process. However, the experiments have some inherent limitations, as they can only obtain the macroscopic adsorption properties but fail to depict the microscopic molecular details which are crucial for revealing fundamental adsorption mechanisms (Wang et al. 2021; Zhang et al. 2022b). In this regard, molecular simulation methods including molecular dynamics (MD) and GCMC have been used extensively to investigate the fundamental mechanisms of CO_2/CH_4 adsorption phenomena at the molecular level by explicitly considering the intermolecular and pore-wall interactions (Sun et al. 2017; Wang et al. 2018; Pang et al. 2019; Hu et al. 2019; Li and Sun 2022; Zhou et al. 2023). The experimental observations in shale nanopores can be effectively explained and supported by simulation results through the analysis of the surface distribution properties of gas molecules. While molecular simulation methods demonstrate superior performances in elucidating adsorption mechanisms, most of the adsorption simulations are conducted in one single nanopore; therefore, it cannot reflect the complex interconnected multiscale pore structure of shale (Wu et al. 2017; Fan et al.

2022). In addition, molecular simulation is typically limited to a small scale, usually within several nanometers, due to computational constraints.

Compared with molecular simulation methods focusing on simple regular pore structure, pore-scale numerical simulations can effectively capture the physical and chemical processes in large-scale realistic porous media with complex pore morphology and topology (Soulaine et al. 2017; Chen et al. 2022; Cai et al. 2022; Wang et al. 2023a). Among these methods, the LBM is one of the most popular approaches (Zheng et al. 2018; Zhang et al. 2020c, 2021; Samanta et al. 2022; Wang et al. 2022b; Wu et al. 2023). However, because the LBM is a mesoscopic method, it is challenging to precisely describe the interaction forces between the adsorbent and gas molecules, making it difficult to accurately consider the adsorption effects. To address the limitations of both approaches while retaining their advantages, the molecular simulation coupled LBM scheme is widely used to model gas flow and transport in shale porous media (Wang et al. 2022a). For example, Zhao et al. (2016) applied the LB model to study CH_4 adsorption by introducing the gas-solid interaction forces determined by the GCMC simulations. Li et al. (2016) used LBM to study methane adsorption and its effect on fluid flow in shale matrix by adopting the pressure-dependent thickness of the adsorbed layer based on MD results. Hou et al. (2020) combined the MD and LBM methods to simulate shale gas transport in the inorganic and organic pore including the slippage boundary condition and gas adsorption effects. Zhou et al. (2022b) coupled MD simulation results with the LBM by introducing a local adsorption density parameter. Based on this, the effects of the adsorption layer and surface diffusion on gas flow and transport behaviors in nanoporous shale matrix are investigated. Liu et al. (2021) explained the adsorption behavior by modifying the force in the LB model, and MD simulation was used as the basic data to make the simulation results more accurate. Then, Liu et al. (2023) extended the single-component model to the multicomponent LB model and then modified the LB parameters by GCMC simulation results to simulate the adsorption behaviors of CH_4 and CO_2 in porous media. However, this work did not consider the increase or decrease in competitive adsorption density of CH_4 and CO_2 caused by the superposition of gas-solid forces in the complex pore structure, and there is a certain error in the calculation of the final adsorption amount. To the best of our knowledge, the coupled molecular simulation–LBM scheme is currently limited to single-component gas adsorption in 2D porous media and has not yet been used to investigate the CO_2/CH_4 competitive adsorption in complex 3D porous media, which is crucial for efficient CO_2-EGR.

Kerogen is the dominant organic component, and illite is one of the typical clay minerals in shale reservoirs. In this study, we proposed a GCMC-LBM coupled simulation scheme incorporating rock-fluid interactions to study CO_2/CH_4 gas mixture adsorption behaviors in 3D kerogen and illite nanoporous media at 333 K and 20 MPa. The adsorption amount, recovery efficiency, and influencing factors are carefully discussed. First, GCMC simulations are carried out to calculate the adsorption density distribution curves of CO_2 and CH_4 in the slit-shaped kerogen and illite pores with varying CO_2 molar fractions. Subsequently, the LB simulations are conducted under the same conditions to obtain the fluid-solid interaction parameter by fitting it with the molecular simulation results. Finally, we performed LB simulations in the 3D porous model based on the fitted parameters to investigate the CO_2/CH_4 competitive adsorption.

Methodology

Molecular Simulation Method. We adopted kerogen monomers (Type II-D) proposed by Ungerer et al. (2015) to model the organic matter in shale rocks. The detailed construction procedure of kerogen nanopores can be found in our previous simulation work (Zhang et al. 2023). Although the polymer consistent force field+ (PCFF+) was used previously to test the physical properties of the kerogen matrix, it adopted a 6-9 Lennard-Jones (LJ) potential form to describe the nonbonded interaction between atoms. However, most of the commonly used force fields (such as TraPPE) are developed based on an LJ form of 12-6, leading to compatibility issues when mixed with PCFF+. Thus, we decided to apply the consistent valence force field (CVFF) by Dauber-Osguthorpe et al. (1988) to describe the potential parameters of kerogen since it has been successfully used to reveal gas adsorption mechanisms in kerogen substrate (Michalec and Lísal 2017; Chong et al. 2021). To validate the force field parameter of CVFF, we simulated the bulk density of kerogen matrices via a series of annealing processes, and the calculated density (1.34 ± 0.028 g/cm³) agreed well with previously reported experimental results ($1.30\sim1.40$ g/cm³) (Okiongbo et al. 2005), thus demonstrating the excellent reliability of the CVFF.

Illite is a typical 2:1 type clay mineral with a unit cell formula of $Si_2AlO_5(OH)$, the coordinate of which is obtained from the previous work (Lee and Guggenheim 1981). Due to the isomorphic substitution effects, Si^{4+} is substituted by Al^{3+} in the tetrahedral sheet creating negatively charged surfaces compensated by K^+ (Chen et al. 2018) and thus resulting in a unit cell of $K(Si_7Al)Al_4O_{20}(OH)_4$. Each illite layer is constructed with $8\times4\times1$ unit cells, leading to a clay sheet of ~4.13 nm×3.59 nm in the *x-y* dimension. Two illite sheets are stacked parallel to build slit-like illite nanopores. The CLAYFF force field developed by Cygan et al. (2004) is used to model illite. CLAYFF is widely used to simulate the structure of a variety of model hydroxide, oxyhydroxide, and clay phases. The force field parameter is optimized and validated by comparing it with experimental and spectroscopic findings in terms of bulk structures, relaxed surface structures, and intercalation processes. CLAYFF has proved to be an effective and reliable force field for modeling fluid interaction with clay phases (e.g., gas adsorption and hydration structure).

The slit-shaped nanopores with a pore size of 4 nm are designed to simulate gas adsorption because it is large enough for a gas component to reach the bulk density in the middle of the pore. The pore width is calculated based on the helium adsorption method as commonly used in previous studies (Tian et al. 2017; Li et al. 2020). The CH_4 and CO_2 molecules are described by TraPPE force field (Martin and Siepmann 1998; Potoff and Siepmann 2001). TraPPE force field demonstrates a high degree of accuracy in the prediction of thermophysical properties (such as vapor-liquid coexistence curves, critical point, diffusion coefficients, and so on) of various gas components (CH_4, CO_2, etc.), making it one of the few force fields generally suitable for studying phase equilibrium and surface adsorption.

To verify the force field of CH_4 and CO_2, we conducted a series of GCMC simulations to calculate the bulk density of single (CH_4 or CO_2) and binary (CO_2-CH_4) systems as reported in previous work (Alafnan 2022; Liu et al. 2023). The simulated results present good agreements with the National Institute of Standards and Technology data (Lemmon et al. 2013) and Peng-Robinson equation of state predictions (Peng and Robinson 1976) (see **Fig. 1**), proving the reliability of the simulation method and force field parameters. The nonbonded force field parameters of CH_4, CO_2, and illite are listed in **Table 1**.

The GCMC simulations were conducted to investigate gas adsorption using the MCCCS Towhee software (version 8.1.0; Martin 2013). In GCMC simulations, the confined fluids inside nanopores are assumed to connect with an infinite large bulk reservoir, and the same chemical potential is achieved at equilibrium. The bulk densities were calculated based on the Peng-Robinson equation of state (Peng and Robinson 1976), and the chemical potentials at corresponding thermophysical conditions were calculated by the Widom insertion method (Widom 1963) using NVT Monte Carlo (MC) simulations. To study the effects of CO_2 concentration on CH_4 displacement efficiency, we set a series of z_{CO_2} equaling 0, 0.1, 0.2, 0.3, 0.4, and 0.5. During GCMC simulations, insertion/deletion, and translation, MC moves are attempted for CH_4, whereas for CO_2 rotational moves are additionally implemented. A total number of 40,000 MC cycles per fluid molecule is carried out for each pressure condition, with the first 15,000 MC cycles used for the equilibrium and the subsequent 25,000 MC cycles for the data sampling. The typical equilibrium snapshots of kerogen and illite nanopores filled with CO_2 and CH_4 are
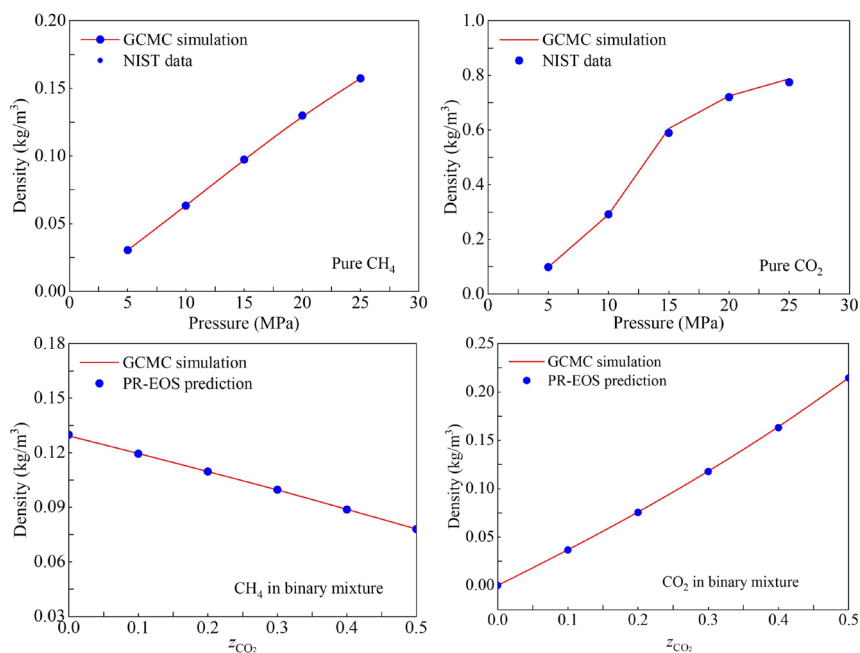
Fig. 1—Bulk density comparison between GCMC simulation results and NIST data for the pure gas component at a range of pressures (5–25 MPa) and Peng-Robinson equation of state predictions for binary mixtures with varying CO_2 molar fractions (0, 0.1, 0.2, 0.3, 0.4, and 0.5) at 20 MPa and 333 K.

Molecules	Atoms	ε(K)	σ(nm)	q(e)
CH_4 (Martin and Siepmann 1998)	C	148	0.373	0
CO_2 (Potoff and Siepmann 2001)	C	27	0.28	+0.7
	O	79	0.305	−0.35
Illite (Cygan et al. 2004)	st	0.000926	0.3302	+2.1
	b	78.2	0.3165	−1.05
	bts	78.2	0.3165	−1.16875
	h	78.2	0.3165	−0.95
	ho	0	0	+1.05
	ao	0.000669	0.4271	+1.575
	at	0.000926	0.3302	+1.575
	K	50.3	0.3334	+1

Table 1—Force field parameters of CH_4, CO_2, and illite.

shown in **Fig. 2.** During GCMC simulations, the LJ potentials are calculated within a cutoff distance of 1.2 nm and the electrostatic interactions are computed by the Ewald summation methods with a k_{alp} value of 5 and a k_{max} value of 10 (Zhang et al. 2023). 3D periodic boundary conditions are applied, and all the atoms in the kerogen and illite are kept fixed in all simulation scenarios.

LB Model. In this paper, the single-relaxation-time multiphase and multicomponent Shan-Chen LBM is proposed to simulate and investigate the competitive adsorption behaviors of CO_2 and CH_4 in 3D nanoporous media by modifying the fluid-fluid and fluid-solid interaction force parameters from molecular simulations. The evolution equation of CO_2 and CH_4 is

$$f_{\sigma,\alpha}\left(\mathbf{x}+\mathbf{e}_\alpha\delta_t, t+\delta_t\right) - f_{\sigma,\alpha}\left(\mathbf{x},t\right) = -\frac{1}{\tau}\left[f_{\sigma,\alpha}\left(\mathbf{x},t\right) - f_{\sigma,\alpha}^{eq}\left(\mathbf{x},t\right)\right], \tag{1}$$

where $f_{\sigma,\alpha=0,1,2,\ldots,18}\left(\mathbf{x},t\right)$ is the density distribution of α direction and σ component (represent CO_2 and CH_4); $\mathbf{x}$ is the spatial position; t is the time; $\mathbf{e}_\alpha$ is the velocity in the α direction; δ_t is the timestep; τ is the relaxation time; and $f_{\sigma,\alpha}^{eq}$ is the equilibrium density distribution:

$$f_{\sigma,\alpha}^{eq} = w_\alpha \rho_\sigma \left[1 + \frac{\mathbf{e}_\alpha \cdot \mathbf{u}_{\sigma,t}}{c_s^2} + \frac{\left(\mathbf{e}_\alpha \cdot \mathbf{u}_{\sigma,t}\right)^2}{2c_s^4} - \frac{\mathbf{u}_{\sigma,t}^2}{2c_s^2}\right], \tag{2}$$

where w_α is the weight factors of α direction; $\rho_\sigma = \sum_\alpha f_{\sigma,\alpha}$ is the density; and $c_s = \frac{1}{\sqrt{3}}$ is the sound speed.
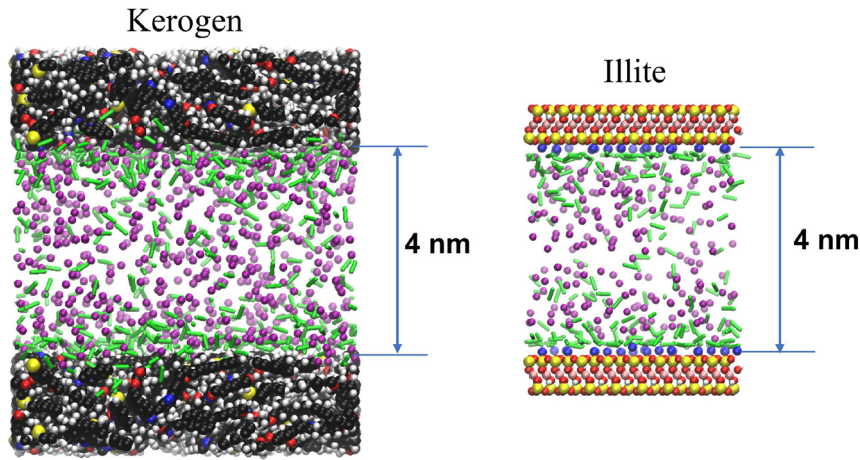
Fig. 2—Equilibrium snapshots of CO_2 and CH_4 distribution inside kerogen and illite nanopores having a pore size of 4 nm (CO_2 molar fraction is $z_{CO_2} = 0.3$). Color scheme—black: C; blue: N in kerogen and K^+ in illite; yellow: Si in illite and S in kerogen; red: O atoms; white: H; pink: Al. The purple ball and green stick represent CH_4 and CO_2 molecules, respectively.

The $\mathbf{u}_{\sigma,t}$ is given by

$$\mathbf{u}_{\sigma,t} = \frac{\sum_\sigma \sum_\alpha \mathbf{e}_\alpha f_{\sigma,\alpha}/\tau_\sigma}{\sum_\sigma \rho_\sigma/\tau_\sigma} + \tau \frac{\left(\mathbf{F}_{\sigma,\text{int}} + \mathbf{F}_{\sigma,\text{ads}} + \mathbf{F}_{\sigma,b}\right)}{\rho_\sigma}, \tag{3}$$

where $\mathbf{F}_{\sigma,\text{int}}$ is the interaction force between different phases:

$$\mathbf{F}_{\sigma,\text{int}}\left(\mathbf{x}, t\right) = -\psi_\sigma\left(\mathbf{x}, t\right) G_{\sigma\bar{\sigma}} \sum_\alpha w_\alpha \psi_{\bar{\sigma}}\left(\mathbf{x} + \mathbf{e}_\alpha \delta_t\right) \mathbf{e}_\alpha, \tag{4}$$

where $G_{\sigma\bar{\sigma}}$ is the interaction strength and can be applied to capture the CO_2/CH_4 miscibility; in this work, $G_{\sigma\bar{\sigma}} = 0$ and $\psi_\sigma\left(\mathbf{x}, t\right) = 1 - \exp\left(-\rho_\sigma\right)$ is the pseudopotential.

$\mathbf{F}_{\sigma,\text{ads}}$ is the interaction force between gas and solid surface, which can be assumed as decreasing exponentially with the distance from the pore walls to capture the density profile of CO_2/CH_4 competitive adsorption effects (Benzi et al. 2006; Zhang et al. 2020b):

$$\mathbf{F}_{\sigma,\text{ads}}\left(\mathbf{x}, t\right) = -G_{\sigma s}\psi\left(\mathbf{x}, t\right) \sum_\alpha e^{-\mathbf{x}_\alpha/\lambda} \mathbf{e}_\alpha, \tag{5}$$

where $G_{\sigma s}$ is a parameter controlling the strength of gas-solid force, and CO_2 and CH_4 correspond to G_{CO_2} and G_{CH_4}, respectively; $\mathbf{x}_\alpha$ is the distance from the wall in direction α; λ is a parameter controlling the trend of the density distribution curve (Feng et al. 2018), and the values are equal to 0.4 nm and 0.6 nm in kerogen and illite pores, respectively, to ensure the accurate density distribution trend.

Simulation Procedures. Fig. 3 illustrates the workflow of the simulations. First, GCMC simulations are performed to calculate the CO_2/CH_4 density distributions in the single 4-nm-slit kerogen and illite nanopores under various conditions. Subsequently, the LB simulations are conducted to obtain the gas-solid interaction parameters (G_{CO_2} and G_{CH_4}) by fitting them with the molecular simulation results. The fitting details will be introduced in the "LB Parameter Fitting in Single Nanopores" section. Then, we generate a 30×30×30 nm³ cubic porous media having complicated pore-throat structure and broad pore size distributions (PSDs) ranging from 1 nm to 12 nm to mimic the realistic morphology of shale pores. Such a PSD is dominant in the typical shale reservoirs (Chalmers et al. 2012). To explore the aperture effects, we designed two kinds of porous media that present the same pore volume but different average pore sizes (4 nm vs. 6 nm). Then, LB simulations in the 3D porous model based on the fitted parameters are carried out, and in the simulation process, based on the bulk density of CO_2 and CH_4 (ρ_{bulk,CO_2} and ρ_{bulk,CH_4}), the initial density of CO_2 and CH_4 in porous media is determined through several iterations to ensure the simulated temperature and pressure. Finally, the effects of mineral type, CO_2 concentration, and pore structure on competitive adsorption behaviors are simulated and discussed.

Results and Discussion

In LB simulation, the physical and lattice units can be converted into each other by length scale (L_0), mass scale (M_0), and time scale (T_0). According to length scale and mass scale, the relationship between physical density and lattice density is $\rho_{\text{physical}} = \rho_{\text{lattice}} M_0/L_0^3$, and according to length scale and time scale, the relationship between physical kinematic viscosity and lattice kinematic viscosity is $v_{\text{physical}} = v_{\text{lattice}} L_0^2/T_0$. In our following simulation, the length scale is first artificially set to $L_0 = 2 \times 10^{-10}$ m, and then the mass scale and time scale can be calculated by referring to the physical and lattice densities and viscosity of the water phase. The physical and lattice densities of the water are equal to $\rho_{w-\text{physical}} = 1000$ kg/m³ and $\rho_{w-\text{lattice}} = 1$, respectively, and the kinematic viscosity of the water is $v_{w-\text{physical}} = 1 \times 10^{-6}$ m²s and $v_{w-\text{lattice}} = 0.1$, respectively. Then, the mass scale in our simulation can be calculated by $M_o = \rho_{w-\text{physical}} L_0^3/\rho_{w-\text{lattice}} = 8 \times 10^{-27}$ kg, and the time scale is calculated by $T_o = v_{w-\text{lattice}} L_0^2/v_{w-\text{physical}} = 4 \times 10^{-15}$ seconds.
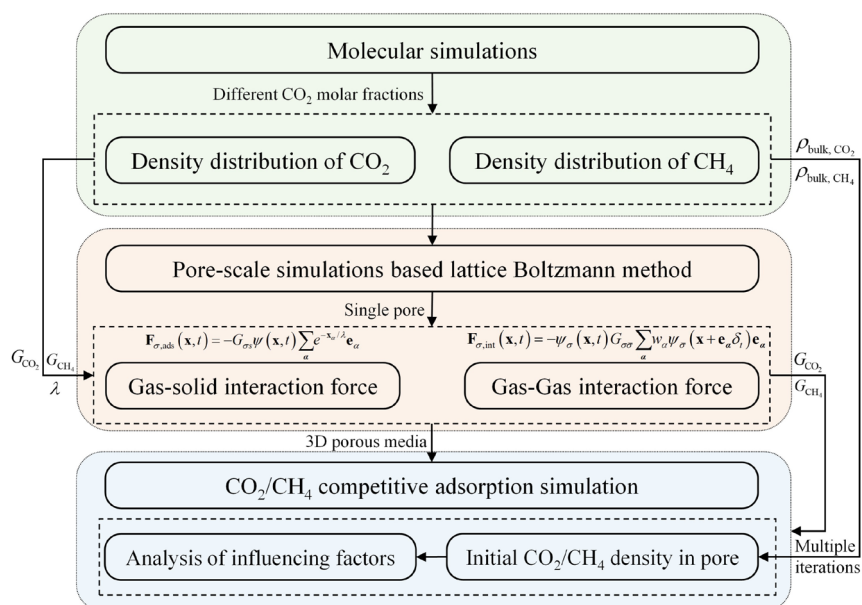
Fig. 3—Workflow of simulation procedures.

LB Parameter Fitting in Single Nanopores. To capture the adsorption effects and extend the simulation scope to a large-scale porous media, we proposed a coupled scheme by fitting molecular simulation results with LBM. GCMC is believed to be an accurate molecular simulation method to evaluate gas adsorption capacity in nanopores (Chen et al. 2018; Hu et al. 2019; Chong et al. 2021), thus adopted as the basis for adsorption curve fitting in this work. According to GCMC results (dots) shown in **Figs. 4 and 5,** in both kerogen and illite nanopores, CH_4 molecules are effectively displaced from the surface region by CO_2, agreeing well with the published molecular simulation results (Chen et al. 2018; Zhang et al. 2020a). Moreover, compared with kerogen, CO_2 presents higher adsorption peaks on illite surfaces because of the stronger interaction with negatively charged surfaces [as also observed in our previous work (Zhang et al. 2023)], showing excellent credibility of our GCMC simulation results.
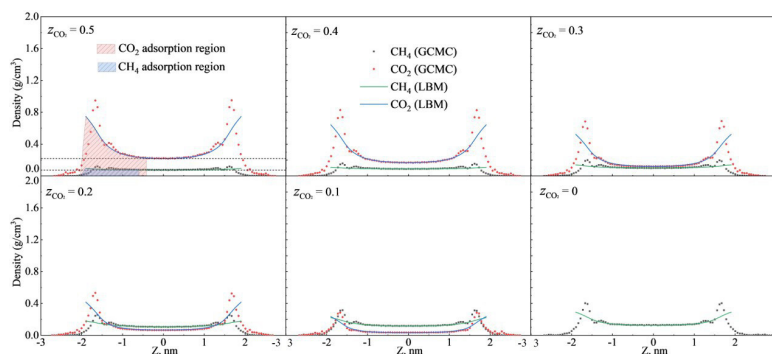

Fig. 4—CO_2 and CH_4 density profiles and LB fitting curves with varying CO_2 concentrations in 4-nm kerogen slit nanopores at 333.15 K and 20 MPa. $Z = 0$ denotes the center position of the nanopores. The black dashed lines correspond to the bulk density.
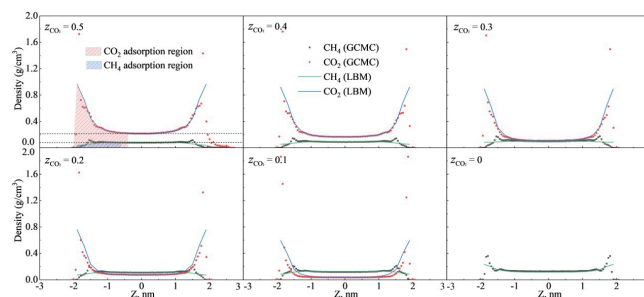

Fig. 5—CO_2 and CH_4 density profiles and LB fitting curves with varying CO_2 concentrations in 4-nm illite slit nanopores at 333.15 K and 20 MPa. $Z = 0$ denotes the center position of the nanopores. The black dashed lines correspond to the bulk density.

Based on GCMC simulations, the averaged densities of CO_2 and CH_4 inside single nanopores with varying CO_2 molar fractions are calculated (see **Table 2**), which are used as the input variables in the subsequent LB simulation at the same conditions. In such a way, we can guarantee the same total gas loadings (i.e., adsorption amount) in GCMC and LB models. Specifically, the area enclosed by the density distribution curves using LBM is equivalent to that with GCMC simulations. Then, the regression process is implemented by adjusting the interaction parameter (G_{CO_2} or G_{CH_4}) between the substrate with each gas component until the bulk density obtained by LB simulations is perfectly equal to that calculated by GCMC simulations. Therefore, by adjusting the gas-solid interaction force while keeping the adsorption amount constant, the LB model proposed in this paper can not only capture the surface adsorption effects but also predict the competitive adsorption behaviors well. Note that here we only presented the adsorption results in the slit pore spaces while gas absorbed inside the ultrasmall nanopores of the bulk kerogen matrix is not taken into consideration. The LB fitting curves in the kerogen and illite single nanopores are clearly shown in **Figs. 4 and 5**, and the corresponding fitted parameters are summarized in **Table 2**, which is used in the following LB competitive adsorption simulation in 3D porous media. The above fitting process and the parameters in **Table 2** are all based on one pressure condition (i.e., 20 MPa); however, the methodology can be applied to fit the density distribution and simulate the competitive adsorption under any pressure conditions. Our work aims to propose an upscaling method bridging the molecular and pore-scale phenomenon by coupling the advantages of molecular simulation and LBM. While the pressure plays an important role in determining the fluid distribution, it is not the focus of this work. Therefore, only one pressure condition is considered in our work.

	Kerogen				Illite			
z_{CO_2}	$\bar{\rho}_{CH_4}$ (g/cm³)	$\bar{\rho}_{CO_2}$ (g/cm³)	G_{CH_4}	G_{CO_2}	$\bar{\rho}_{CH_4}$ (g/cm³)	$\bar{\rho}_{CO_2}$ (g/cm³)	G_{CH_4}	G_{CO_2}
0	0.171	0	−0.055	−0.085	0.144	0	−0.090	−0.245
0.1	0.148	0.083	−0.059	−0.087	0.119	0.151	−0.090	−0.245
0.2	0.130	0.153	−0.06	−0.094	0.107	0.215	−0.090	−0.245
0.3	0.113	0.225	−0.050	−0.083	0.095	0.274	−0.090	−0.245
0.4	0.096	0.293	−0.046	−0.082	0.083	0.331	−0.075	−0.215
0.5	0.081	0.361	−0.046	−0.081	0.071	0.389	−0.052	−0.195

Table 2—Fluid-solid interaction parameters in LB simulation fitted from GCMC.

In practice, experimental studies usually get excess adsorption while it is quite difficult to obtain absolute adsorption, exactly what we are concerned about. Fortunately, the adsorbed phase can be easily identified through atomic density distribution curves, thus making it possible to calculate the absolute adsorption amount. Combined with the density distribution curve, the adsorption region is defined as the shadow area (see **Figs. 4 and 5**) from the pore surface to the location where the fluid density starts to deviate from the bulk value in the middle of the pore. With this criterion, the CO_2 and CH_4 adsorption regions with a thickness of ~1.6 nm and 1.4 nm in kerogen and illite pores are determined, respectively. It should be noted that the thickness is independent of the CO_2 concentration and surface types after carefully checking each case, so we used identical values to identify the adsorbed phase for all the simulation scenarios. Accordingly, the fluid quantity within the adsorption region is classified as the absolute adsorption amount, which is mainly discussed in this work.

Then, based on LB parameters fitted in 4-nm slit pores, we carried out competitive adsorption simulation in 2-nm kerogen and illite slit pores, and the CO_2 molar fraction equals 0.5. The simulation results are shown in **Fig. 6,** and the LB simulation results agree well with molecular simulation results, indicating that the competitive adsorption simulation in porous media with complex pore structure and multi-aperture characteristics can be carried out based on the above fitting parameters in **Table 2**. From **Fig. 6**, it is found that the CO_2 adsorption on illite surfaces is much higher than that on kerogen surfaces, indicating a stronger interaction between CO_2 and illite surfaces. This finding is quite meaningful and useful in the context of CGS in subsurface conditions. For example, based on our simulation results, illite mineral presents higher CO_2 surface adsorption, which means that more CO_2 can be stored in illite nanopores compared with kerogen. Therefore, it is suggested to choose the illite-rich rather than kerogen-rich depleted reservoir to sequester CO_2 in the CGS project.
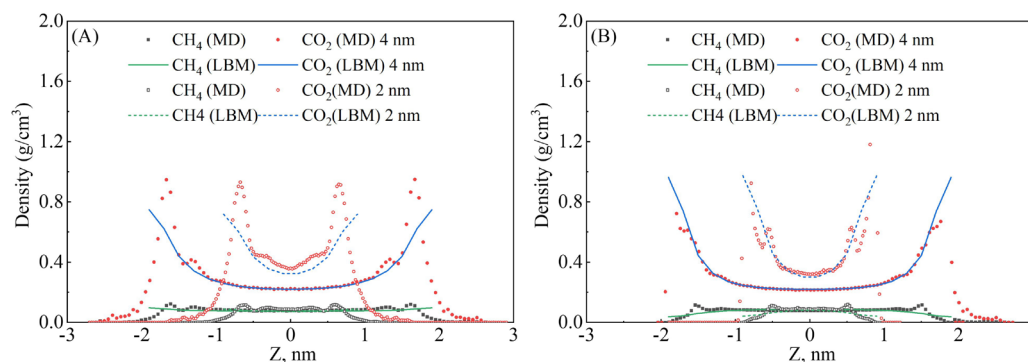

Fig. 6—CO_2 and CH_4 density profiles and LB fitting curves in 4-nm and 2-nm slit nanopores at 333.15 K and 20 MPa for (A) kerogen and (B) illite. The CO_2 molar fraction equals 0.5.

CO_2/CH_4 Competitive Adsorption Behaviors in 3D Porous Media. Based on the gas-solid interaction parameters listed in **Table 2**, CO_2/CH_4 competitive adsorption simulations with LBM are performed in the 3D porous substrate, bridging a gap between the single-

slit nanocompetitive adsorption behaviors in 3D porous mediapores and large-scale porous media. For the 3D porous media used in our simulation, the construction process is as follows (Rabbani and Jamshidi 2014; Rabbani et al. 2014; Rabbani and Babaei 2021). First, the 150×150×150 grids are constructed, and 0–1 values are generated randomly in each grid **(Fig. 7A).** Then, Gaussian filtering is used to filter random 0–1 values in the 3D image, and the filtered image is shown in **Fig. 7B**. Following, the separation of solid matrix and pore-throat space is realized by setting threshold value, and the 3D porous media diagram obtained is shown in **Fig. 7C**. Finally, the watershed algorithm is used to divide the pore-throat space **(Fig. 7D)**, and the PSD can be calculated **(Fig. 7E)**.
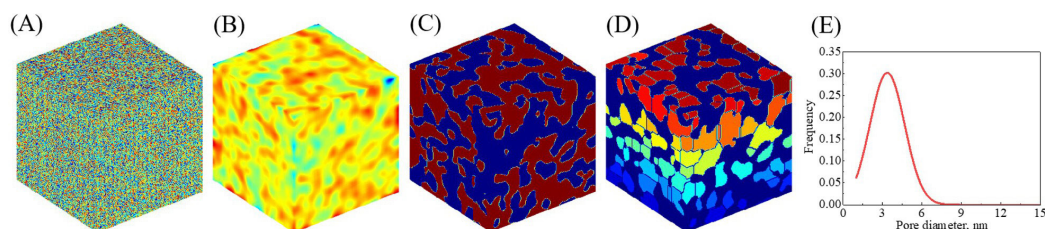

Fig. 7—Porous media construction process (Rabbani and Jamshidi 2014; Rabbani et al. 2014; Rabbani and Babaei 2021). (A) Random 0–1 values. (B) Gaussian filter. (C) 3D porous media; red represents solid and blue represents pore-throat space. (D) The pore-throat structure is segmented by the watershed algorithm. (E) PSD.

As illustrated in **Fig. 8,** two porous media—A_L and B_S—with the same pore volume but different pore structures are constructed based on the above method. Based on PSD results, the averaged pore diameters of these two porous media are calculated as 5.4 nm and 3.4 nm, respectively. The lattice size of porous media is 150×150×150, corresponding to a physical size of 30×30×30 nm^3 with the length scale $L_0 = 2 \times 10^{-10}$ m. Periodic boundary conditions are applied for each direction of the porous media. While the shale porosity is generally reported to be less than 10% (Klaver et al. 2015), to ensure the simulation connectivity, the porosity of these two porous media adopted in our simulation is set at the same value of 50%.
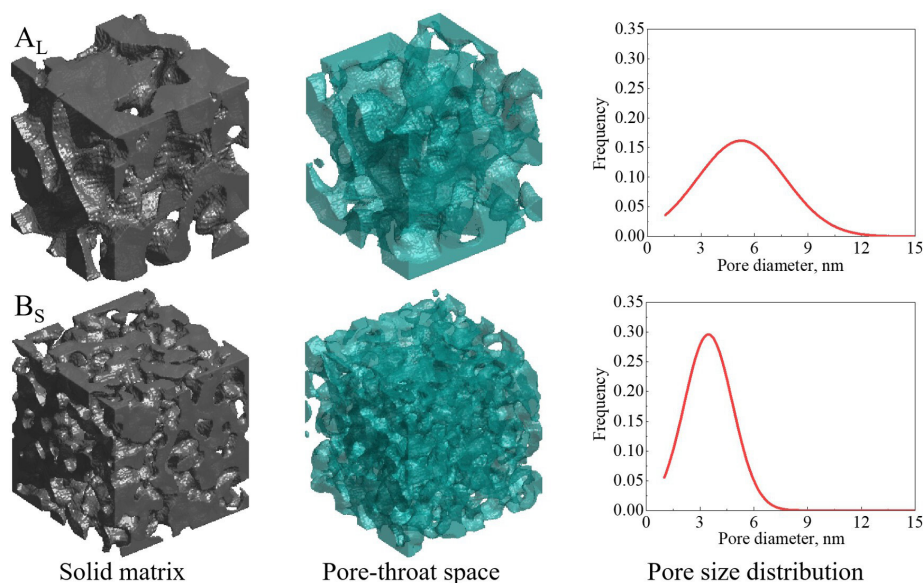

Fig. 8—Skeleton and internal pore structure of two kinds of porous media and corresponding PSD. The subscripts L and S denote the porous media with large and small averaged pore sizes, respectively.

Due to the complex pore structure, using the average density of CO_2 and CH_4 obtained from 4-nm slit pores as the input in the porous media may not guarantee that the bulk fluid density matches the target values at the corresponding thermophysical conditions (i.e., bulk density shown in **Fig. 1**). Therefore, a series of trial-and-error tests is necessary. First, the average densities of CO_2 and CH_4 obtained in slit pores are given as the initial settings at each grid to carry out the LB simulations in 3D porous media using the fitted gas-solid interaction force parameters. After achieving equilibrium, the bulk and adsorbed gas regions are determined according to the criteria proposed in the "LB Parameter Fitting in Single Nanopores" section. Consequently, the average density of the bulk gas can be calculated. If the calculated bulk gas density is greater or smaller than the desired values at a certain pressure and temperature, then adjust the density values at each grid until the relative error of equilibrated bulk density between the porous media and slit pores is within 2%.

Fig. 9 shows the 3D spatial density distributions in two kinds of kerogen porous media with $z_{CO_2} = 0.3$. The results show that both CO_2 and CH_4 tend to accumulate in the near-wall region due to surface adsorption effects, while CO_2 presents stronger surface adsorption over CH_4. In the corner areas (as circled in **Fig. 9**), owing to the overlapping of gas-solid interaction forces, the adsorption strength is enhanced. Overall, the LB simulation results in 3D porous media demonstrate consistent competitive adsorption behaviors with our molecular simulation observations, again validating the accuracy of GCMC-coupled LBM in simulating CO_2/CH_4 mixture adsorption. To further quantitatively investigate CO_2 and CH_4 adsorption capacity, we calculated the adsorption amount of each component inside kerogen and illite porous media having different pore structures with various CO_2 molar fractions in CO_2/CH_4 mixtures as shown in **Figs. 10 and 11.**
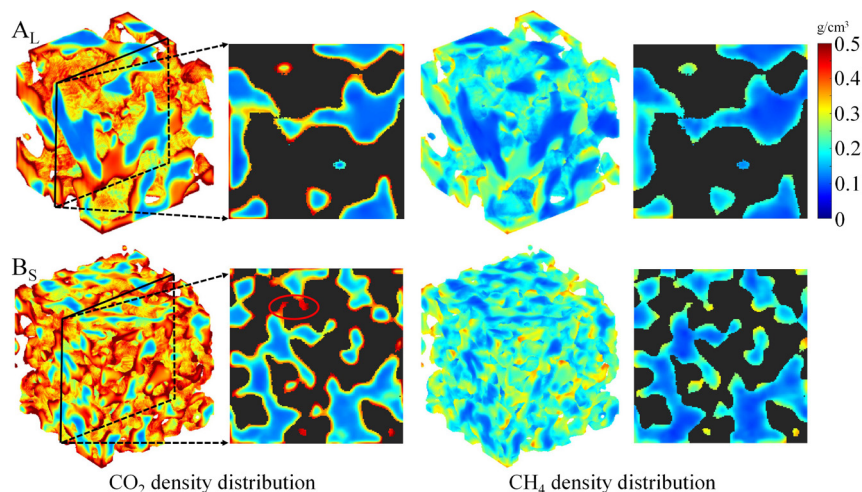
Fig. 9—3D spatial density distribution and slice map of CO_2 and CH_4 in two kinds of porous media (x_{CO_2} = 0.3). The slice graph is generated by cutting along the plane in the middle of the porous media. The black areas in the slice graph represent the rock substrate.
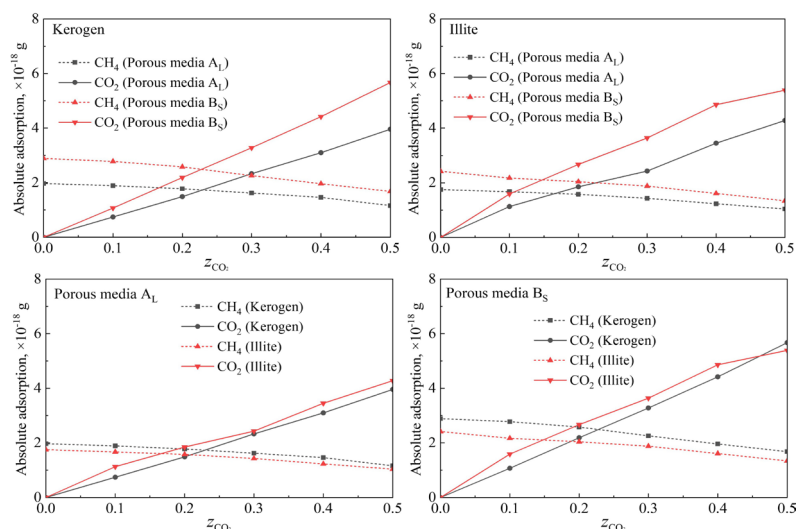

Fig. 10—CO_2 and CH_4 adsorption amount vs. CO_2 molar fraction in kerogen and illite porous media.
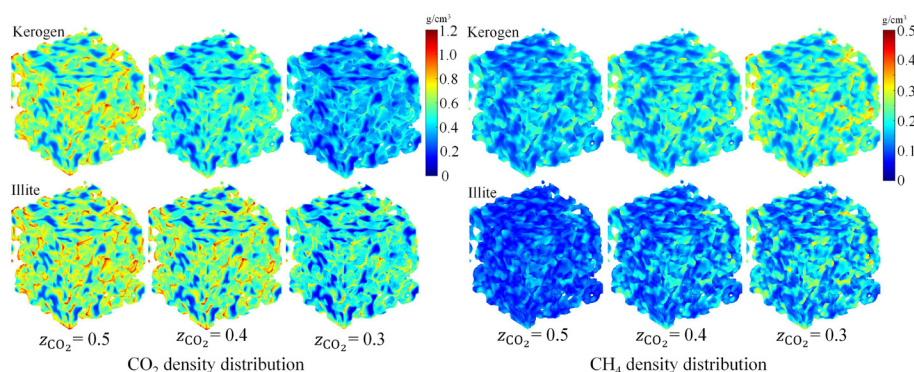

Fig. 11—3D spatial distribution of CO_2 and CH_4 in kerogen and illite porous media (Bs) with different CO_2 concentrations.

As we expected, with the increase in CO_2 concentration, the adsorption amount of CH_4 gradually decreases due to the surface competitive adsorption with CO_2. As shown in **Fig. 10**, in both kerogen and illite media, we notice that the red lines (Porous Media B_S) are always above the black lines (Porous Media A_L), indicating that the porous media with a narrower pore size causes a higher adsorption amount. It is mainly because when pore volume is equal, the porous media with smaller pore sizes has larger surface areas, thus providing more available adsorption sites. On the other hand, the adsorbed phase in smaller pores accounts for a larger proportion of the total gas content,
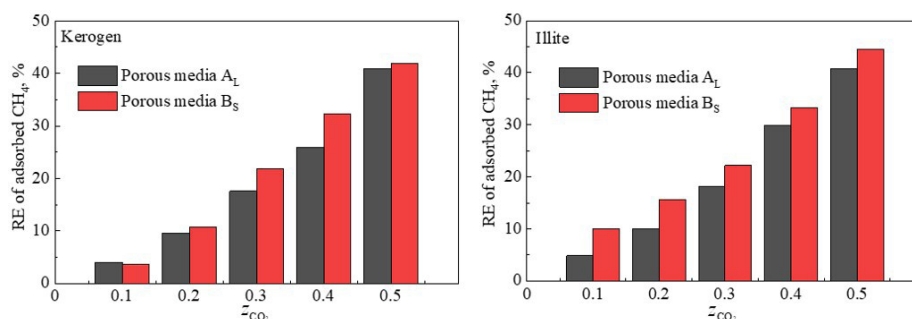
Fig. 12—RE of adsorbed CH_4 vs. CO_2 molar fraction in two kinds of porous media.
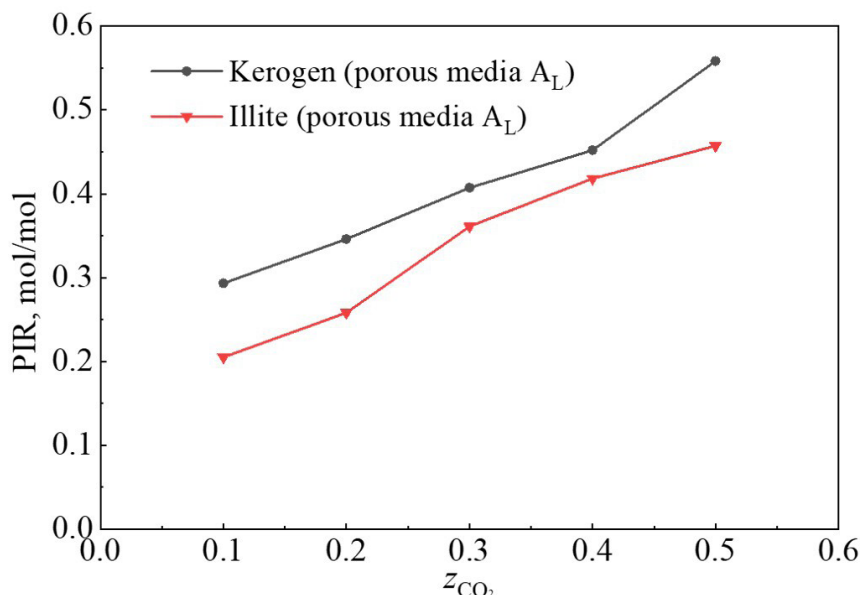

Fig. 13—PIR vs. CO_2 molar fraction in two kinds of porous media.

which might also contribute to promoting the adsorption amount. Compared with kerogen porous media, CH_4 presents lower adsorption capacity in illite media, which is in line with the weaker adsorption peak of CH_4 in the vicinity of the illite surface as shown in **Figs. 4 and 5**. This is also supported by the 3D spatial distribution results in **Fig. 11**, in which the suppressed CH_4 surface adsorption is clearly recognized in illite porous media. By contrast, a higher CO_2 adsorption amount is generally observed in illite porous media, consistent with the GCMC simulation observations depicted in **Figs. 4 and 5**, which is well evidenced by the enhanced CO_2 surface adsorption in illite porous media as shown in **Fig. 11**.

CH_4 Recovery and Production Efficiency in 3D Porous Media. To provide a better understanding for quantitatively estimating how much adsorbed CH_4 can be produced, we calculated the recovery efficiency (RE) of adsorbed CH_4 at different conditions as shown in **Fig. 12,** which is given as follows:

$$\text{RE} = \frac{m_{aCH_4}^0 - m_{aCH_4}^i}{m_{aCH_4}^0} \times 100\%, \qquad (6)$$

where RE is the recovery efficiency of adsorbed CH_4, $m_{aCH_4}^0$ is the adsorption amount of CH_4 in porous media in the absence of CO_2 (i.e., $z_{CO_2} = 0$), and $m_{aCH_4}^i$ represents the adsorption amount of CH_4 in porous media at a certain CO_2 concentration. It is not surprising that in both kerogen and illite porous media, the RE gradually increases as z_{CO_2} rises from 0.1 to 0.5, because of enhanced surface competitive adsorption of CO_2 at high concentrations. Meanwhile, we found that the RE of adsorbed CH_4 in porous media with a small aperture is slightly greater than that with a large aperture. It is because the CO_2/CH_4 adsorption selectivity is increased with decreasing pore size, resulting in a lower CH_4 content in the adsorbed phase in smaller pores, thereby favorable for enhancing CH_4 recovery. In addition, we noticed that the RE of adsorbed CH_4 in illite porous media is slightly greater than that in kerogen, mainly attributed to the strengthened surface adsorption of CO_2 with a strong quadrupole moment [1.367×10^{-39} C·m² (Müller and Gelb 2003)] on negatively charged illite surfaces, showing good agreements with our GCMC simulation results discussed in the "LB Parameter Fitting in Single Nanopores" section.

As RE calculation considers only the production of CH_4 while ignoring the CO_2 injection, it thus cannot truly reflect the CO_2-EGR efficiency. Consequently, we proposed the production-injection ratio (PIR) to better characterize the CO_2 replacement efficiency by calculating the ratio between produced CH_4 and injected CO_2, which is defined as

$$PIR = \frac{m^0_{aCH_4}/M_{CH_4} - m^i_{aCH_4}/M_{CH_4}}{m^i_{aCO_2}/M_{CO_2}}, \tag{7}$$

where PIR is the production-injection ratio, $m^i_{aCO_2}$ represents the adsorption amount of CO_2 in porous media for a certain CO_2 concentration, and M_{CH_4} and M_{CO_2} refer to the molar mass of CH_4 and CO_2, respectively. A higher PIR value indicates that more adsorbed CH_4 is recovered per CO_2 adsorbed. As observed in **Fig. 13,** the PIR values increase monotonically with increasing CO_2 concentration, indicating that CH_4 molecules are easier to desorb from the surfaces at higher CO_2 content. Contrary to RE, the PIR in kerogen porous media is slightly higher than that in illite. The possible reason is that the surface adsorption of CH_4 on illite surfaces is weaker than it is on kerogen (smaller numerator), while CO_2 adsorption on illite surfaces is much stronger (larger denominator), thus leading to reduced PIR values in illite porous media.

Conclusions

In this study, we integrated the GCMC and LB simulations to examine CO_2/CH_4 competitive adsorption behaviors in 3D shale kerogen and illite porous media. The effects of CO_2 concentrations, pore structure, and surface types were carefully discussed. The competitive adsorption behaviors of CO_2 and CH_4 in 3D nanoporous media can be accurately captured in LB simulation by adjusting CO_2-solid and CH_4-solid interaction forces based on the atomic density distribution results calculated with GCMC simulation. The consistent adsorption behaviors between molecular simulations and LBM sufficiently proved the credibility of our proposed GCMC-coupled LBM simulation scheme. Specifically, the porous media with narrower pore sizes cause higher adsorption amounts (in both CO_2 and CH_4) due to the larger surface areas and a higher proportion of the adsorbed phase in smaller pores. Compared with kerogen porous media, CO_2 presents a stronger adsorption capacity in illite porous media while the surface adsorption of CH_4 is reduced. Meanwhile, the RE of adsorbed CH_4 is enhanced in the porous media with a smaller pore width because of increased CO_2/CH_4 adsorption selectivity. Interestingly, while the RE of adsorbed CH_4 in illite porous media is greater than that in kerogen, an opposite trend is observed in the PIR data.

Our work gives an in-depth understanding of CO_2/CH_4 competitive adsorption in shale nanoporous media and proposes an upscaling method bridging the molecular-scale and pore-scale phenomena by coupling the advantages of molecular simulations and LBM. However, several limitations should be acknowledged. The realistic shale formation is characterized by a broad PSD, including both micropores (<2 nm) and mesopores (2–50 nm) in the kerogen matrix (Wang et al. 2015; Psarras et al. 2017; Li et al. 2024). The micropores contribute to the porosity and adsorption in the shale rocks as well, but this work only focuses on the mesopores neglecting the micropores (especially the gas absorbed inside the ultrasmall nanopores of the bulk kerogen matrix). In addition, we constructed the nanoporous media consisting of one single mineral, but in practice, organic and clay nanopores coexisted in shale reservoirs. Future research should comprehensively consider all the existing nanopores to improve the accuracy and applicability of the simulation models.

Declaration of Competing Interest

The authors declare that they have no known competing financial interests or personal relationships that could have appeared to influence the work reported in this paper.

Acknowledgment

References

Alafnan, S. 2022. Adsorption–Desorption Hysteresis in Shale Formation: New Insights into the Underlying Mechanisms. *Energy Fuels* 36 (10): 5307–5315. https://doi.org/10.1021/acs.energyfuels.2c00444.

Bekeshov, D., Ashimov, S., Wang, Y. et al. 2023. Understanding Gas-Enhanced Methane Recovery in Graphene Nanoslits via Molecular Simulations. *Capillarity* 6 (1): 1–12. https://doi.org/10.46690/capi.2023.01.01.

Benzi, R., Biferale, L., Sbragaglia, M. et al. 2006. Mesoscopic Two-Phase Model for Describing Apparent Slip in Micro-Channel Flows. *Europhys Lett* 74 (4): 651–657. https://doi.org/10.1209/epl/i2006-10022-0.

Cai, J., Wood, D. A., Hajibeygi, H. et al. 2022. Multiscale and Multiphysics Influences on FLuids in Unconventional Reservoirs: Modeling and Simulation. *Adv Geo-Energy Res* 6 (2): 91–94. https://doi.org/10.46690/ager.2022.02.01.

Chalmers, G. R., Bustin, R. M., and Power, I. M. 2012. Characterization of Gas Shale Pore Systems by Porosimetry, Pycnometry, Surface Area, and Field Emission Scanning Electron Microscopy/Transmission Electron Microscopy Image Analyses: Examples from the Barnett, Woodford, Haynesville, Marcellus, and Doig Units. *AAPG Bulletin* 96 (6): 1099–1119. https://doi.org/10.1306/10171111052.

Chen, L., He, A., Zhao, J. et al. 2022. Pore-Scale Modeling of Complex Transport Phenomena in Porous Media. *Prog Energy Combust Sci* 88: 100968. https://doi.org/10.1016/j.pecs.2021.100968.

Chen, G., Lu, S., Liu, K. et al. 2018. GCMC Simulations on the Adsorption Mechanisms of CH_4 and CO_2 in K-Illite and Their Implications for Shale Gas Exploration and Development. *Fuel* 224: 521–528. https://doi.org/10.1016/j.fuel.2018.03.061.

Chong, L., Sanguinito, S., Goodman, A. L. et al. 2021. Molecular Characterization of Carbon Dioxide, Methane, and Water Adsorption in Micropore Space of Kerogen Matrix. *Fuel* 283: 119254. https://doi.org/10.1016/j.fuel.2020.119254.

Cooper, J., Stamford, L., and Azapagic, A. 2016. Shale Gas: A Review of the Economic, Environmental, and Social Sustainability. *Energy Tech* 4 (7): 772–792. https://doi.org/10.1002/ente.201500464.

Curtis, J. B. 2002. Fractured Shale-Gas Systems. *AAPG Bulletin* 86 (11): 1921–1938. https://doi.org/10.1306/61EEDDBE-173E-11D7-8645000102C1865D.

Cygan, R. T., Liang, J.-J., and Kalinichev, A. G. 2004. Molecular Models of Hydroxide, Oxyhydroxide, and Clay Phases and the Development of a General Force Field. *J Phys Chem B* 108 (4): 1255–1266. https://doi.org/10.1021/jp0363287.

Dauber-Osguthorpe, P., Roberts, V. A., Osguthorpe, D. J. et al. 1988. Structure and Energetics of Ligand Binding to Proteins: Escherichia Coli Dihydrofolate Reductase-Trimethoprim, a Drug-Receptor System. *Proteins* 4 (1): 31–47. https://doi.org/10.1002/prot.340040106.

Fan, Y., Liu, K., Yu, L. et al. 2022. Assessment of Multi-Scale Pore Structures and Pore Connectivity Domains of Marine Shales by Fractal Dimensions and Correlation Lengths. *Fuel* 330: 125463. https://doi.org/10.1016/j.fuel.2022.125463.

Feng, D., Li, X., Wang, X. et al. 2018. Capillary Filling of Confined Water in Nanopores: Coupling the Increased Viscosity and Slippage. *Chem Eng Sci* **186**: 228–239. https://doi.org/10.1016/j.ces.2018.04.055.

Hou, P., Gao, F., He, J. et al. 2020. Shale Gas Transport Mechanisms in Inorganic and Organic Pores Based on Lattice Boltzmann Simulation. *Energy Rep* **6**: 2641–2650. https://doi.org/10.1016/j.egyr.2020.09.021.

Hu, X., Deng, H., Lu, C. et al. 2019. Characterization of CO_2/CH_4 Competitive Adsorption in Various Clay Minerals in Relation to Shale Gas Recovery from Molecular Simulation. *Energy Fuels* **33** (9): 8202–8214. https://doi.org/10.1021/acs.energyfuels.9b01610.

Jung, J. W., Espinoza, D. N., and Santamarina, J. C. 2010. Properties and Phenomena Relevant to CH_4-CO_2 Replacement in Hydrate-bearing Sediments. *J. Geophys. Res: Solid Earth* **115** (B10). B10102. https://doi.org/10.1029/2009JB000812.

Klaver, J., Desbois, G., Littke, R. et al. 2015. BIB-SEM Characterization of Pore Space Morphology and Distribution in Postmature to Overmature Samples from the Haynesville and Bossier Shales. *Mar Pet Geol* **59**: 451–466. https://doi.org/10.1016/j.marpetgeo.2014.09.020.

Klewiah, I., Berawala, D. S., Alexander Walker, H. C. et al. 2020. Review of Experimental Sorption Studies of CO_2 and CH_4 in Shales. *J Nat Gas Sci Eng* **73**: 103045. https://doi.org/10.1016/j.jngse.2019.103045.

Kuuskraa, V., Stevens, S. H., Moodhe, K. D. et al. 2013. Technically Recoverable Shale Oil and Shale Gas Resources: An Assessment of 137 Shale Formations in 41 Countries Outside the United States, US Energy Information Administration, US Department of Energy, Washington, DC, USA. https://www.eia.gov/analysis/studies/worldshalegas/pdf/overview.pdf.

Lee, J. H. and Guggenheim, S. 1981. Single Crystal X-Ray Refinement of Pyrophyllite-1 Tc. *Am Mineral* **66** (3–4): 350–357.

Lemmon, E. W., Huber, M. L., and McLinden, M. O. 2013. NIST Standard Reference Database 23. Reference Fluid Thermodynamic and Transport Properties (REFPROP), Version 9. Gaithersburg, Maryland, USA: National Institute of Standards and Technology, US Department of Commerce.

Li, W., Cao, J., Liang, Y. et al. 2024. Molecular Simulation of Methane/Ethane Mixture Adsorption Behavior in Shale Nanopore Systems with Micropores and Mesopores. *Fuel* **358**: 130294. https://doi.org/10.1016/j.fuel.2023.130294.

Li, Z. and Elsworth, D. 2019. Controls of CO_2–N_2 Gas Flood Ratios on Enhanced Shale Gas Recovery and Ultimate CO_2 Sequestration. *J Pet Sci Eng* **179**: 1037–1045. https://doi.org/10.1016/j.petrol.2019.04.098.

Li, Z.-Z., Min, T., Kang, Q. et al. 2016. Investigation of Methane Adsorption and Its Effect on Gas Transport in Shale Matrix through Microscale and Mesoscale Simulations. *Int J Heat Mass Transf* **98**: 675–686. https://doi.org/10.1016/j.ijheatmasstransfer.2016.03.039.

Li, W., Nan, Y., Zhang, Z. et al. 2020. Hydrophilicity/Hydrophobicity Driven CO2 Solubility in Kaolinite Nanopores in Relation to Carbon Sequestration. *J Chem Eng* **398**: 125449. https://doi.org/10.1016/j.cej.2020.125449.

Li, J. and Sun, C. 2022. How Gas Recovery and Carbon Storage Capacity Response to Dynamic Deformation of Kerogen upon CO_2/CH_4 Competitive Adsorption for CCUS? Evidence from Molecular Dynamics. *Int J Coal Geol* **263**: 104113. https://doi.org/10.1016/j.coal.2022.104113.

Liao, Q., Zhou, J., Xian, X. et al. 2023. Competition Adsorption of CO_2/CH_4 in Shale: Implications for CO_2 Sequestration with Enhanced Gas Recovery. *Fuel* **339**: 127400. https://doi.org/10.1016/j.fuel.2023.127400.

Liu, L., Wang, Y., and Aryana, S. A. 2021. Insights into Scale Translation of Methane Transport in Nanopores. *J Nat Gas Sci Eng* **96**: 104220. https://doi.org/10.1016/j.jngse.2021.104220.

Liu, J., Xie, L., Elsworth, D. et al. 2019. CO_2/CH_4 Competitive Adsorption in Shale: Implications for Enhancement in Gas Production and Reduction in Carbon Emissions. *Environ Sci Technol* **53** (15): 9328–9336. https://doi.org/10.1021/acs.est.9b02432.

Liu, L., Zhao, Y., Luo, M. et al. 2023. Bridging Adsorption Behavior of Confined CH_4-CO_2 Binary Mixtures across Scales. *Fuel* **354**: 129310. https://doi.org/10.1016/j.fuel.2023.129310.

Lyu, Q., Tan, J., Li, L. et al. 2021. The Role of Supercritical Carbon Dioxide for Recovery of Shale Gas and Sequestration in Gas Shale Reservoirs. *Energy Environ Sci* **14** (8): 4203–4227. https://doi.org/10.1039/D0EE03648J.

Martin, M. G. 2013. MCCCS Towhee: A Tool for Monte Carlo Molecular Simulation. *Mol Simul* **39** (14–15): 1212–1222. https://doi.org/10.1080/08927022.2013.828208.

Martin, M. G. and Siepmann, J. I. 1998. Transferable Potentials for Phase Equilibria. 1. United-Atom Description of N-Alkanes. *J Phys Chem B* **102** (14): 2569–2577. https://doi.org/10.1021/jp972543+.

Michalec, L. and Lísal, M. 2017. Molecular Simulation of Shale Gas Adsorption onto Overmature Type II Model Kerogen with Control Microporosity. *Mol Phys* **115** (9–12): 1086–1103. https://doi.org/10.1080/00268976.2016.1243739.

Middleton, R. S., Gupta, R., Hyman, J. D. et al. 2017. The Shale Gas Revolution: Barriers, Sustainability, and Emerging Opportunities. *Appl Energy* **199**: 88–95. https://doi.org/10.1016/j.apenergy.2017.04.034.

Müller, E. A. and Gelb, L. D. 2003. Molecular Modeling of Fluid-Phase Equilibria Using an Isotropic Multipolar Potential. *Ind Eng Chem Res* **42** (17): 4123–4131. https://doi.org/10.1021/ie030033y.

Okiongbo, K. S., Aplin, A. C., and Larter, S. R. 2005. Changes in Type II Kerogen Density as a Function of Maturity: Evidence from the Kimmeridge Clay Formation. *Energy Fuels* **19** (6): 2495–2499. https://doi.org/10.1021/ef050194+.

Pang, W., He, Y., Yan, C. et al. 2019. Tackling the Challenges in the Estimation of Methane Absolute Adsorption in Kerogen Nanoporous Media from Molecular and Analytical Approaches. *Fuel* **242**: 687–698. https://doi.org/10.1016/j.fuel.2019.01.059.

Peng, D.-Y. and Robinson, D. B. 1976. A New Two-Constant Equation of State. *Ind Eng Chem Fund* **15** (1): 59–64. https://doi.org/10.1021/i160057a011.

Potoff, J. J. and Siepmann, J. I. 2001. Vapor–Liquid Equilibria of Mixtures Containing Alkanes, Carbon Dioxide, and Nitrogen. *AIChE J* **47** (7): 1676–1682. https://doi.org/10.1002/aic.690470719.

Psarras, P., Holmes, R., Vishal, V. et al. 2017. Methane and CO_2 Adsorption Capacities of Kerogen in the Eagle Ford Shale from Molecular Simulation. *Acc Chem Res* **50** (8): 1818–1828. https://doi.org/10.1021/acs.accounts.7b00003.

Qin, X., Singh, H., and Cai, J. 2022. Sorption Characteristics in Coal and Shale: A Review for Enhanced Methane Recovery. *Capillarity* **5** (1): 1–11. https://doi.org/10.46690/capi.2022.01.01.

Rabbani, A. and Babaei, M. 2021. Image-Based Modeling of Carbon Storage in Fractured Organic-Rich Shale with Deep Learning Acceleration. *Fuel* **299**: 120795. https://doi.org/10.1016/j.fuel.2021.120795.

Rabbani, A. and Jamshidi, S. 2014. Specific Surface and Porosity Relationship for Sandstones for Prediction of Permeability. *Int J Rock Mech Min Sci* **71**: 25–32. https://doi.org/10.1016/j.ijrmms.2014.06.013.

Rabbani, A., Jamshidi, S., and Salehi, S. 2014. An Automated Simple Algorithm for Realistic Pore Network Extraction from Micro-Tomography Images. *J Pet Sci Eng* **123**: 164–171. https://doi.org/10.1016/j.petrol.2014.08.020.

Ross, D. J. K. and Bustin, R. M. 2009. The Importance of Shale Composition and Pore Structure upon Gas Storage Potential of Shale Gas Reservoirs. *Mar Pet Geol* **26** (6): 916–927. https://doi.org/10.1016/j.marpetgeo.2008.06.004.

Safaei-Farouji, M., Misch, D., and Sachsenhofer, R. F. 2023. A Review of Influencing Factors and Study Methods of Carbon Capture and Storage (CCS) Potential in Coals. *Int J Coal Geol* **277**: 104351. https://doi.org/10.1016/j.coal.2023.104351.

Samanta, R., Chattopadhyay, H., and Guha, C. 2022. A Review on the Application of Lattice Boltzmann Method for Melting and Solidification Problems. *Comput Mater Sci* **206**: 111288. https://doi.org/10.1016/j.commatsci.2022.111288.

Soulaine, C., Roman, S., Kovscek, A. et al. 2017. Mineral Dissolution and Wormholing from a Pore-Scale Perspective. *J Fluid Mech* **827**: 457–483. https://doi.org/10.1017/jfm.2017.499.

Sun, H., Zhao, H., Qi, N. et al. 2017. Molecular Insights into the Enhanced Shale Gas Recovery by Carbon Dioxide in Kerogen Slit Nanopores. *J Phys Chem C* **121** (18): 10233–10241. https://doi.org/10.1021/acs.jpcc.7b02618.

Tian, Y., Yan, C., and Jin, Z. 2017. Characterization of Methane Excess and Absolute Adsorption in Various Clay Nanopores from Molecular Simulation. *Sci Rep* **7** (1). 12040. https://doi.org/10.1038/s41598-017-12123-x.

Ungerer, P., Collell, J., and Yiannourakou, M. 2015. Molecular Modeling of the Volumetric and Thermodynamic Properties of Kerogen: Influence of Organic Type and Maturity. *Energy Fuels* **29** (1): 91–105. https://doi.org/10.1021/ef502154k.

Wang, H., Cai, J., Su, Y. et al. 2023a. Pore-Scale Study on Shale Oil-CO_2-Water Miscibility, Competitive Adsorption, and Multiphase Flow Behaviors. *Langmuir* **39** (34): 12226–12234. https://doi.org/10.1021/acs.langmuir.3c01570.

Wang, Q., Chen, X., Jha, A. N. et al. 2014. Natural Gas from Shale Formation – The Evolution, Evidences and Challenges of Shale Gas Revolution in United States. *Renew Sust Energ Rev* **30**: 1–28. https://doi.org/10.1016/j.rser.2013.08.065.

Wang, H., Su, Y., Wang, W. et al. 2022a. CO_2-Oil Diffusion, Adsorption and Miscible Flow in Nanoporous Media from Pore-Scale Perspectives. *J Chem Eng* **450**: 137957. https://doi.org/10.1016/j.cej.2022.137957.

Wang, T., Tian, S., Li, G. et al. 2018. Molecular Simulation of CO_2/CH_4 Competitive Adsorption on Shale Kerogen for CO_2 Sequestration and Enhanced Gas Recovery. *T J Phys Chem C* **122** (30): 17009–17018. https://doi.org/10.1021/acs.jpcc.8b02061.

Wang, T., Tian, S., Li, G. et al. 2021. Molecular Simulation of Gas Adsorption in Shale Nanopores: A Critical Review. *Renew Sust Energ Rev* **149**: 111391. https://doi.org/10.1016/j.rser.2021.111391.

Wang, Y., Tsotsis, T. T., and Jessen, K. 2015. Competitive Sorption of Methane/Ethane Mixtures on Shale: Measurements and Modeling. *Ind Eng Chem Res* **54** (48): 12187–12195. https://doi.org/10.1021/acs.iecr.5b02850.

Wang, H., Wang, W., Su, Y. et al. 2022b. Lattice Boltzmann Model for Oil/Water Two-Phase Flow in Nanoporous Media Considering Heterogeneous Viscosity, Liquid/Solid, and Liquid/Liquid Slip. *SPE J.* **27** (6): 3508–3524. https://doi.org/10.2118/210564-PA.

Wang, W., Xie, Q., An, S. et al. 2023b. Pore-Scale Simulation of Multiphase Flow and Reactive Transport Processes Involved in Geologic Carbon Sequestration. *Earth-Sci Rev* **247**: 104602. https://doi.org/10.1016/j.earscirev.2023.104602.

Widom, B. 1963. Some Topics in the Theory of Fluids. *J Chem Phys* **39** (11): 2808–2812. https://doi.org/10.1063/1.1734110.

Wu, J., Gan, Y., Shi, Z. et al. 2023. Pore-Scale Lattice Boltzmann Simulation of CO2-CH4 Displacement in Shale Matrix. *Energy* **278**. 127991. https://doi.org/10.1016/j.energy.2023.127991.

Wu, T., Li, X., Zhao, J. et al. 2017. Multiscale Pore Structure and Its Effect on Gas Transport in Organic-rich Shale. *Water Resour Res* **53** (7): 5438–5450. https://doi.org/10.1002/2017WR020780.

Wu, J., Shen, L., Huang, P. et al. 2023b. Selective Adsorption and Transport of CO_2–CH_4 Mixture under Nano-Confinement. *Energy* **273**. 127224. https://doi.org/10.1016/j.energy.2023.127224.

Xie, W., Wang, M., Chen, S. et al. 2022. Effects of Gas Components, Reservoir Property and Pore Structure of Shale Gas Reservoir on the Competitive Adsorption Behavior of CO_2 and CH_4. *Energy* **254**. 124242. https://doi.org/10.1016/j.energy.2022.124242.

Zhang, T., Javadpour, F., Li, X. et al. 2020a. Mesoscopic Method to Study Water Flow in Nanochannels with Different Wettability. *Phys Rev E* **102** (1): 013306. https://doi.org/10.1103/PhysRevE.102.013306.

Zhang, T., Javadpour, F., Li, J. et al. 2021. Pore-Scale Perspective of Gas/Water Two-Phase Flow in Shale. *SPE J.* **26** (2): 828–846. https://doi.org/10.2118/205019-PA.

Zhang, T., Javadpour, F., Yin, Y. et al. 2020b. Upscaling Water Flow in Composite Nanoporous Shale Matrix Using Lattice Boltzmann Method. *Water Resour Res* **56** (4). e2019WR026007. https://doi.org/10.1029/2019WR026007.

Zhang, M., Liu, Z., Pan, B. et al. 2023. Molecular Simulation on CO_2/H_2S CO-Adsorption in Organic and Inorganic Shale Nanopores. *Appl Surf Sci* **624**: 157167. https://doi.org/10.1016/j.apsusc.2023.157167.

Zhang, P., Lu, S., and Li, J. 2019. Characterization of Pore Size Distributions of Shale Oil Reservoirs: A Case Study from Dongying Sag, Bohai Bay Basin, China. *Mar Pet Geol* **100**: 297–308. https://doi.org/10.1016/j.marpetgeo.2018.11.024.

Zhang, S., Tang, S., Li, Z. et al. 2022. Effect of Pore Structure on Competitive Sorption and Diffusion of Mixed Methane and Carbon Dioxide in Anthracite, South Qinshui Basin, China. *Int J Coal Geol* **253**: 103956. https://doi.org/10.1016/j.coal.2022.103956.

Zhang, M., Zhan, S., and Jin, Z. 2020c. Recovery Mechanisms of Hydrocarbon Mixtures in Organic and Inorganic Nanopores during Pressure Drawdown and CO_2 Injection from Molecular Perspectives. *J Chem Eng* **382**: 122808. https://doi.org/10.1016/j.cej.2019.122808.

Zhang, Y., Zhu, X., Chu, C. et al. 2022b. Applications of Atomic Force Microscopy-Based Imaging and Force Spectroscopy in Assessing Environmental Interfacial Processes. *Crit Rev Environ Sci Technol* **52** (14): 2421–2452. https://doi.org/10.1080/10643389.2021.1889282.

Zhao, J., Yao, J., Zhang, L. et al. 2016. Pore-Scale Simulation of Shale Gas Production Considering the Adsorption Effect. *Int J Heat Mass Transf* **103**: 1098–1107. https://doi.org/10.1016/j.ijheatmasstransfer.2016.08.026.

Zheng, J., Ju, Y., and Wang, M. 2018. Pore-Scale Modeling of Spontaneous Imbibition Behavior in a Complex Shale Porous Structure by Pseudopotential Lattice Boltzmann Method. J. Geophys. Res: Solid Earth **123** (11): 9586–9600. https://doi.org/10.1029/2018JB016430.

Zhou, S., Wang, H., Li, B. et al. 2022a. Predicting Adsorbed Gas Capacity of Deep Shales under High Temperature and Pressure: Experiments and Modeling. *Adv Geo-Energy Res* **6** (6): 482–491. https://doi.org/10.46690/ager.2022.06.05.

Zhou, J., Xie, S., Jiang, Y. et al. 2018. Influence of Supercritical CO_2 Exposure on CH_4 and CO_2 Adsorption Behaviors of Shale: Implications for CO_2 Sequestration. *Energy Fuels* **32** (5): 6073–6089. https://doi.org/10.1021/acs.energyfuels.8b00551.

Zhou, W., Yang, X., and Liu, X. 2022b. Multiscale Modeling of Gas Flow Behaviors in Nanoporous Shale Matrix Considering Multiple Transport Mechanisms. *Phys Rev E* **105** (5): 055308. https://doi.org/10.1103/PhysRevE.105.055308.

Zhou, J., Zhang, C., and Ranjith, P. G. 2023. Behaviours of Methane and Water in Heterogeneous Shale Nanopores: Effect of Water Saturation and Pore Size. *Fuel* **335**: 126675. https://doi.org/10.1016/j.fuel.2022.126675.